International Communications in Heat and Mass Transfer 124 (2021) 105271

Contents lists available at ScienceDirect

International Communications in Heat and Mass Transfer

journal homepage: www.elsevier.com/locate/ichmt

Experimental study on thermal contact resistance of carbon fiber reinforced silicon carbide composite with 3D needled preform (3DN C/SiC)

Xing-Jie Ren [a], Hao Ding [a], Yan-Jun Dai [a], Jian-Yong Tu [b], Xu Chen [b], Jiang-Yi He [b], Wen-Quan Tao [a,*]

[a] Key Laboratory of Thermo-Fluid Science and Engineering of MOE, School of Energy and Power Engineering, Xi'an Jiaotong University, Xi'an, Shaanxi 710049, China
[b] Xi'an Golden Mountain Ceramic Composites, Xi'an, Shaanxi, China

ARTICLE INFO

Keywords:
Thermal contact resistance
Thermal properties
3 DN C/SiC composite

ABSTRACT

In this paper, thermal contact resistance (TCR) of three different contacts of a composite are experimentally investigated when the contact interfaces are filled with air. The surface roughnesses of the three contacts are 0.95/16.91 μm (Contact A, titanium alloy/composite), 9.54/9.73 μm (Contact B, composite/composite), and 11.53/6.85 μm (Contact C, composite/titanium alloy). The measured TCRs of the three contacts decrease with an increase in loading pressure and interface temperature. For Contact B, the effect of temperature on thermal contact resistance gradually decreases with an increasing loading pressure. For Contact C when loading pressure increases to 3.6 MPa, the decreasing trend of the thermal contact resistance with increasing loading pressure becomes mild. Additionally, experimental uncertainties are analyzed and calculated.

1. Introduction

Thermal contact resistance (TCR) significantly influences the efficiency of heat dissipation and the safety of engineering apparatuses, especially in a situation of high heat flux. It is a bottleneck that restricts accurate thermal management and cooling performance in many applications, such as cryogenics, aircraft industry, nuclear industry, space vehicles, microelectronics industry, and nanoscale technology, etc.

Previous studies pointed out that thermal contact resistance is a comprehensive problem that researches should take following aspects into considerations: material surface topography, contact mechanics and deformation, material mechanical properties and thermal conductivity [1,2], especially when constructing analytical models or conducting numerical simulations. In addition, experimental studies also show that thermal contact resistance can be affected by loading pressure and service temperature. Studies on thermal contact resistance have been conducted since 1920 s [3] and investigation approaches can be mainly divided into analytical models [4–12], numerical simulations [2,13–18] and experimental studies [19–29]. Experimental studies can be divided into two kinds of steady-state and transient measurements.

For the transient approach, IR camera is often used to record temperatures to determine thermal contact resistance. Burghold and Kneer [30,31] studied the time-dependent contact heat transfer using high-speed IR-thermography to record the temperature changes. In their research, specimens were heated up to different temperatures separately and then brought into contact. It should be noted that temperatures of all specimens were less than 100 °C in their research. Zhu et al. [32] investigated the transient contact heat transfer between 300 M steel and 5CrNiMo, and the effects of the initial temperature of the 300 M specimen, the interfacial pressure, the oxide layer and the graphite lubricant on thermal contact resistance were evaluated. Vu et al. [29] investigated the contact heat transfer coefficients in nonisothermal glass molding by using transient method.

Steady-state approach based on 1D heat conduction theory is the most common method to determine thermal contact resistance. Generally, two cylindrical specimens are brought into contact, and then different loading pressures and temperatures are imposed to the specimens. The temperatures of the specimens can be recorded by thermocouples or IR thermography. The heat flux through the specimens can be measured by two ways: one uses the temperatures measured in three positions of the specimen, and the other is measured by two heat flux meter bars using Fourier's law of heat conduction [33]. The meter bars can be constructed from relatively high conductivity materials with well documented thermal conductivity within the temperature range of interest. They should also have a relatively high thermal stability, a good surface flatness, and a high hardness in high temperature and loading pressure. Besides, the cross section of the meter bars should be identical

* Corresponding author.
E-mail address: wqtao@mail.xjtu.edu.cn (W.-Q. Tao).

https://doi.org/10.1016/j.icheatmasstransfer.2021.105271

Available online 20 April 2021

Nomenclature

a	Thermal diffusivity
c_p	Specific heat capacity
h	Thermal contact conductance
P	Loading pressure
q	Heat flux
R	Thermal contact resistance
Ra	Average surface roughness
T	Temperature
$u(R)$	Standard uncertainty of TCR
$U(R)$	Relative uncertainty of TCR
x, y, z	Cartesian coordinates
ρ	Density
λ	Thermal conductivity

with the specimens. Using the method of heat flux meter bars can overcome the weakness of the missing or inaccurate thermal conductivity of the specimens. In addition, when the height of the test specimen cannot be high enough to include three measurement positions for temperature, the heat flux meter bar should be used to determine the heat flux. Although it imposes additional thermal resistance between specimens and heat flux meter bars, it doesn't affect the measurement results of the specimens. Cousineau et al. [26] experimentally measured the thermal conductivity of electromagnetic steel lamination materials and determined the thermal contact resistance between laminations in a stack, as well as factors affecting contact resistance between laminations, such as the contact pressure and surface finish. In their research, heat flux was determined by copper metering blocks with resistance temperature detectors (RTDs), and the blocks were located on the top and bottom of the test sample. Le et al. [27] designed experiments to study the thermal contact resistance as well as the effective thermal conductivity of low thermal conductivity fibrous insulation material at high temperatures and in atmospheric conditions by using Ti-6Al-4 V alloys as heat flux meter bars. They found that TCR contributed to the total thermal resistance of the fibrous specimens is approximately 42% and 35%, respectively, when the average temperature of the specimen is 190 °C and 290 °C. Toebben et al. [34] experimentally investigated the oxidation influence on the thermal contact resistance at the blade-rotor-connection in a steam turbine under a vacuum condition. In their study, heat fluxes were determined by thermocouples located at the blade and rotor themselves. Utilizing the steady state approach and heat flux measured by heat flux meters (HT-50 thermal flux meters from ITI, Inc. USA), Tariq and Asif [35] conducted experiments to investigate thermal contact conductance of three materials (copper, brass and stainless steel) in a vacuum environment (~6 Pa) under different pressures and roughness, and the temperature of the specimen was less than 100 °C in their research.

The material studied in this paper is carbon fiber reinforced silicon carbide composite with 3D needled preform (3DN C/SiC). It is a functional-structural material that is widely used in the advanced brake system of vehicles because of its low cost, high strength, high coefficient of static friction, etc. However, after a search for literature, there is no published experimental studies on thermal contact resistance of this material. Only for some other composites experimental studies for thermal conductivity or thermal contact resistance can be found [36–38]. Hence, it is necessary to experimentally determine thermal contact resistance of this kind of composite.

The rest of the paper is organized as follows. In Section 2 experimental apparatus and methods are introduced. Section 4 devotes to the presentation of results and discussion. In Section 5 uncertainty analysis is provided for the experimental results of TCR, and finally some conclusions are drawn in Section 6.

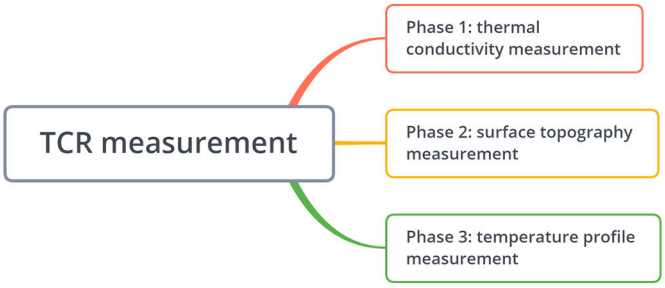

Fig. 1. Experimental phases of TCR.

2. Experimental phases and apparatus

The experiments for determining TCR can be divided into three phases: 1. thermal conductivity measurement; 2. surface topography measurement; 3. temperature profile measurement, as shown in Fig. 1. The details of the three phases are described as follows.

2.1. Thermal conductivity measurement

The temperature-dependent thermal conductivity of the composite is measured by three methods: 1) a Hotdisk platform (TPS 2500S, see Fig. 2); 2) ASTM_E1225–13 method [39]; 3) Laser-flash thermal conducting instrument (LFA457, NETZSCH).

The specimens tested by Hotdisk are two identical cylinders with 10 mm in height and 30 mm in diameter, and the cylindrical specimens used in ASTM_E1225–13 method is 22 mm in height and 48 mm in diameter.

Thermal conductivity measurement using laser thermal conducting instrument method needs to measure the temperature-dependent specific heat capacities firstly. The specific heat capacity is measured by a differential scanning calorimetry (STA449F3-DIL402PC, NETZSCH). Three small block specimens are cut off from one cylindrical composite, and each of the block is nearly 3 mm × 3 mm × 3 mm. It should be noted that the three small blocks were cut off from different positions to alleviate the effect of inequality of fibers and matrix in each specimen and hence to ensure the measurement accuracy of the specific heat capacity.

Then the laser-flash thermal conducting instrument (LFA457, NETZSCH) is used to measure the thermal diffusivity of the composite. The specimen for thermal diffusivity measurement is a thin cylinder with 12.8 mm in diameter and 2.5 mm in height. Finally, densityρ, measured thermal diffusivity a and specific heat capacity c_p are used to calculate thermal conductivityλ, as shown by Eq. (1),

$$\lambda = a\rho c_p \tag{1}$$

2.2. Surface topography measurement

No real surface is perfectly smooth, and it is believed that thermal contact resistance is mainly determined by its actual surface roughness. Therefore, the experimentally-determined thermal contact resistance data are meaningless if the surface topography of the contact interfaces brought into contact is not specified. In our study, we use a microscope (contour GT-K, Bruker, see Fig. 3) to measure the surface topography and select the conventional average surface roughness, denoted by *Ra*, to represent the surface roughness. The microscope uses optical interference principle and the measurement interval is 0.003958 mm in both x and y direction. Besides, it has a 0.1 nm resolution in vertical direction when switching to VSI (Vertical Scanning Interferometry) measurement mode. Because the actual surface area of the specimen is larger than the single measurement area of the objective lens, the entire surface is divided into many small squares by the embedded "stitch function" of the microscope, as shown in Fig. 4. One square needs a single

Fig. 2. TPS 2500S.

Fig. 3. Contour GT microscope.

measurement. Finally, all single measurements are stitched into a complete measured surface topography.

Fig. 5 shows the test specimens and surface roughness measurement results. Fig. 5 (a) shows the two test specimens with 48 mm in diameter and 22 mm in height. Fig. 5 (b) shows the measured surface topography of one specimen. As we can see, the seemingly smooth surface has numerous small valleys and peaks under the microscope. More detailed information can be found in Fig. 5 (c) and Fig. 5 (d) where X,Y profiles mean the asperity distributions along the perpendicularly white lines on the left of Fig. 5 (c).

Table 1 lists the measured average surface roughness of the three contact pairs and the heat flux meter bar. The heat flux meter bars are titanium alloys (Ti-6Al-4 V). Contact A is the pair of titanium alloy/composite. Contact B is composite/composite pair, and contact C is composite/titanium alloy pair.

2.3. Temperature profile measurement

After the measurement of the surface topography, the specimens are brought into contact and installed in the temperature measurement system (see Fig. 6). The system consists of a pressure loading unit, a cooling unit, a heating unit, thermal insulations and a data acquisition unit. The pressure loading unit can provide pressures up to 20 MPa through the displacement load, and the heating unit can provide a temperature up to 1000 °C. The pressure data are acquired by a pressure sensor and saved in the form of electrical signals. The sheathed thermocouples (E type with 2 mm in diameter) are mounted in the holes of the specimens to measure the temperatures at different spots.

The cylindrical specimens are 48 mm in diameter and 22 mm in height. Each specimen has eight holes to mount thermocouples, and every four holes are in the same height and uniformly distributed in the peripheral direction. The diameter of each hole is 2 mm and the depth is 12 mm, as shown in Fig. 7. Because of the inherent limitations in manufacturing process of this material, the height can't be more than 22 mm, hence, only two-layer temperature measurement spots can be maintained in the specimen. For this reason, the heat flux calculated from the specimens is only as a reference, and the titanium alloys (Ti-6Al-4 V) is used as the heat flux meter bars. The thermal conductivity of the titanium alloys (Ti-6Al-4 V) has been accurately measured in previous study, besides, this material keeps a good thermal stability and a relative high hardness in high temperature situation.

To ensure an approximate 1D steady-state heat conduction, both the specimens and the flux meter bars are surrounded by aerogel insulation materials with a very low thermal conductivity to reduce the heat loss in the radial direction to a negligible extent. One end of the specimen is cooled by the recycling coolant. It is circulated water, and its temperature in the cooling unit is kept at 15 °C. The water is pumped from the cooling equipment to cool the specimens and then flows back to the cooling unit. Electrically heating the specimens is finished by a silicon carbide rod placed in the heating furnace. The experimental setup is depicted in Fig. 8 (a), and Fig. 8 (b) shows the schematic of temperature measurement. According to our experiences, the criterion that the specimen temperature has reached a steady state is set as temperature variation being less than 0.3 °C within 30 min. It nearly takes 8 h to reach the steady state. As shown in Fig. 8 (a), two heat flux meter bars are used to measure the heat flux in the vertical direction. The meter bars are titanium alloy (Ti-6Al-4 V) and its temperature-dependent thermal conductivities are known, hence, by using the Fourier's law of heat conduction the heat flux through the contact interfaces can be determined.

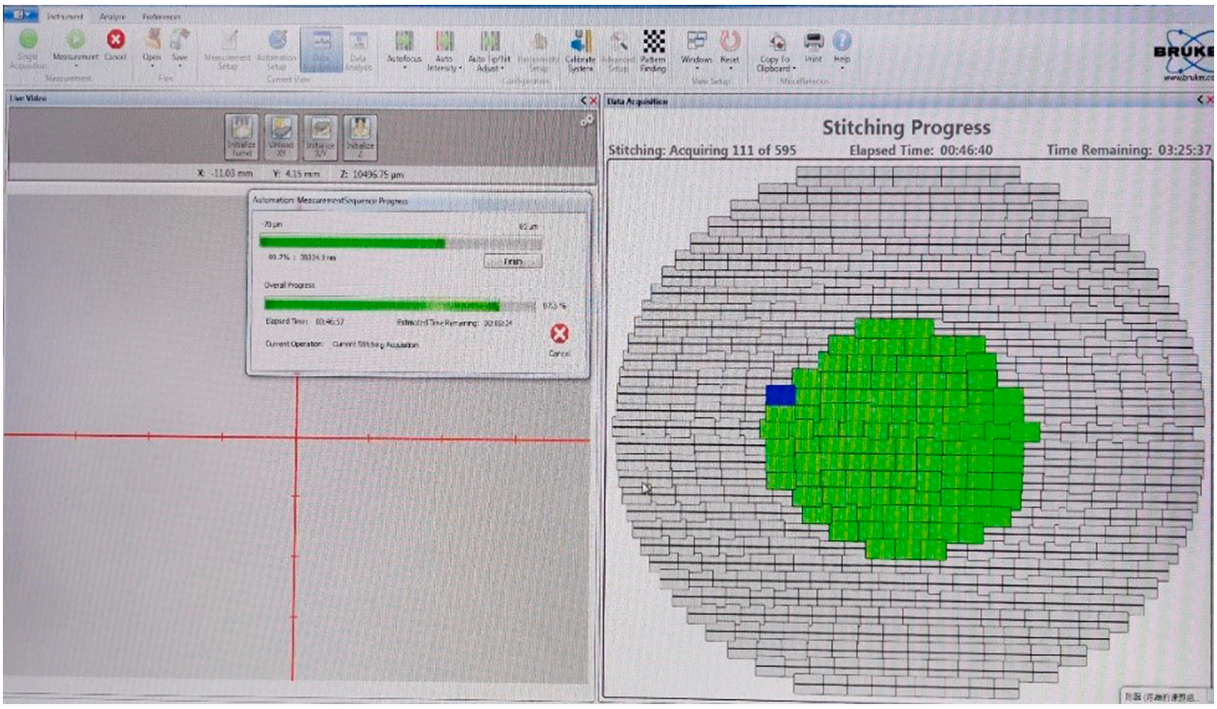

Fig. 4. Stitching progress in surface topography measurement.

When the temperature data under steady state are recorded, using the linear fitting method as depicted in Fig. 8 (b), the interface temperature differences between two contact interfaces can be obtained. It should be mentioned that only when thermal conductivity of the specimens varies with temperature slightly, a linear fitting method can be used to obtain the interface temperatures. Thus, it is necessary to measure the thermal conductivity of the specimen at different temperatures. The average heat flux measured by the two heat flux meter bars is taken as the test heat flux. Accordingly, we can calculate thermal contact resistance by Eq. (2),

$$R = \frac{\Delta T}{q} \tag{2}$$

Similarly, thermal contact resistance between specimens and heat flux meter bars can also be calculated according to the above mentioned method.

3. Experimental results and discussions

3.1. Specific heat capacity

Fig. 9 shows the experimentally measured specific heat capacity of the three small block specimens. It can be seen that the specific heat capacity is strongly temperature-dependent and there are some differences among three measured curves. These differences may be mainly attributed to different proportions of carbon fibers and SiC matrix of each specimen because of their small size. The specific heat capacity of the composite is calculated according to Eq. (3) [40],

$$c_p = \frac{c_{pf} \cdot m_f + c_{pm} \cdot (M - m_f)}{M} \tag{3}$$

where c_{pf} and c_{pm} are the specific heat capacities of the carbon fiber and matrix, respectively. M and m_f are the mass of the composite and the fibers respectively. The arithmetic mean value of three experimental results is taken as the specific heat capacity of the tested composite.

3.2. Thermal diffusivity (through-thickness direction)

The measured thermal diffusivity in through-thickness direction of the composite is presented in Fig. 10, showing a decrease tendency with an increase in temperature. Such variation pattern of the thermal diffusivity in through-thickness direction is consistent with previous studies [41,42].

3.3. Thermal conductivity (through-thickness direction)

In our study, thermal conductivity of the composite is measured by three methods, and Fig. 11 shows the experimental results of the thermal conductivity. It can be seen that all the measurement results varies slightly with an increase in temperature, which is the basis for determining interface temperatures according to the method shown in Fig. 8 (a), ie., within a not large variation range of temperature, say 50–100 °C the specimen thermal conductivity can be regarded as constant hence linear extrapolation for its surface temperature is reasonable.

Table 2 lists the detailed values. In the table, Laser-flash is the experimental results. The data of ASTM over 400 °C and Hotdisk over 300 °C are the extrapolated values from their fitting results for measured data below this temperature. δ_1, δ_2, δ_3 are the deviations of laser-flash method. ASTM method and Hotdisk method compared with mean value of three methods, respectively.

ASTM Standard [33] indicates that thermal conductivity values for the same material measured in different laboratories are expected to be within 18% of the mean of the values, and our results satisfy such a criteria. While it is still necessary to explain the reasons of the deviations among three measurement methods. Apart from the temperature measurement errors, the possible other reasons include following aspects. (1) The size of the specimen used in Hotdisk may be smaller than the ideal size. (2) For the Laser-flash method, the thermal conductivity is calculated with the experimental results of specific heat capacity, thermal diffusivity and density. Such three experimental results are obtained from different specimens. For the composite, different specimens may have different proportions of the carbon fibers and SiC matrix. Hence, the experimental results may scatter in some degree. (3) Fig. 12 shows

(a) The specimens

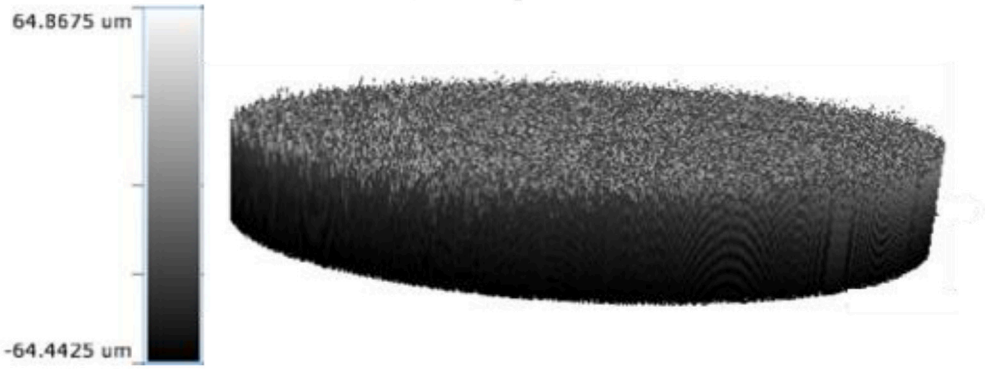

(b) The measured surface topography (3D view)

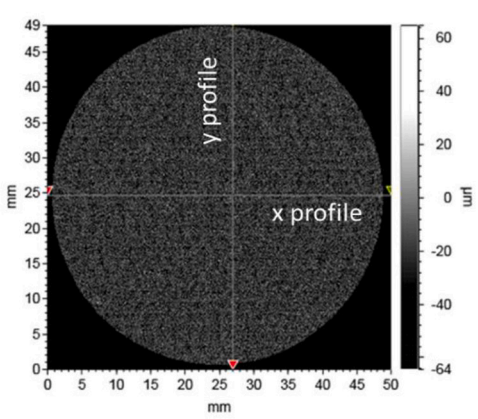

(c) The measure surface topography (top view)

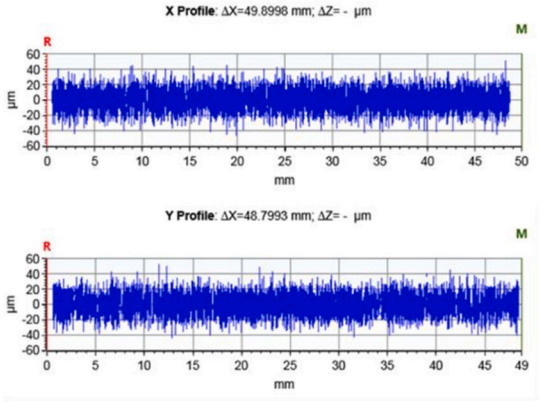

(d) Measured roughness in x and y profile

Fig. 5. Surface topography.

internal structure of the composite measured by a scanning electron microscope (SEM). It reveals that thermal conductivity of this material is anisotropic, strongly direction-dependent and sensitive to the direction in which fibers are oriented. Different test specimen may have different fiber orientation, hence resulting in some differences. Hence, the measurement or numerical prediction of composites thermal conductivity remains a challenging task [40,43–45].

3.4. Temperature profile

Table 3 lists the experimental conditions. The experimental process can be described as follows,

(1) Fix the loading pressure and heating temperature. After reaching a steady state, change the heating temperatures to another value from a lower to a larger one as shown in the first row of Table 3 in sequence.
(2) After finishing one data run, increase the loading pressure to another constant up to the loading pressure of 4.39 MPa and then changing the heating temperatures from 400 °C to 900 °C again.

Fig. 13 shows the temperature profiles of the specimens and heat flux meter bars. It can be seen that the fitting curves of the heat flux meter bars are nearly linear, therefore it is reasonable to use these data to extrapolate the interfaces temperatures by following linear equation.

Table 1
Contact surface roughness.

Name	Material	location	*Ra*/ μm	Contact pair
Heat flux meter bar 1	Titanium alloy	Upper surface	0.95	Contact A
Specimen 1	Needled composite	Lower surface	16.91	
		Upper surface	9.54	Contact B
Specimen 2	Needled composite	Lower surface	9.73	
		Upper surface	11.53	Contact C
Heat flux meter bar 2	Titanium alloy	Lower surface	6.85	

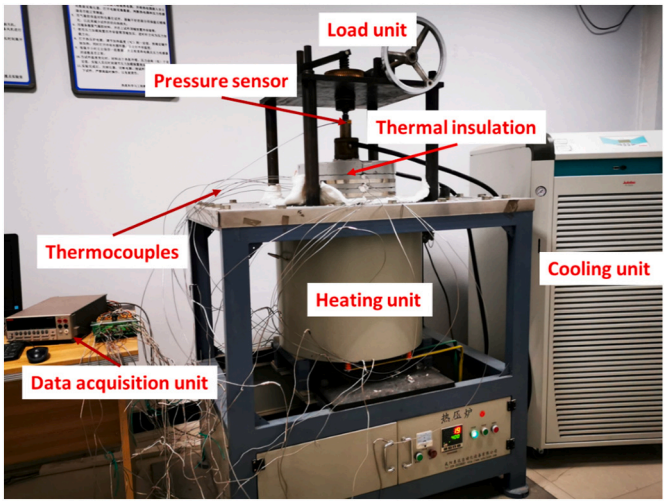

Fig. 6. System for temperature profile measurement.

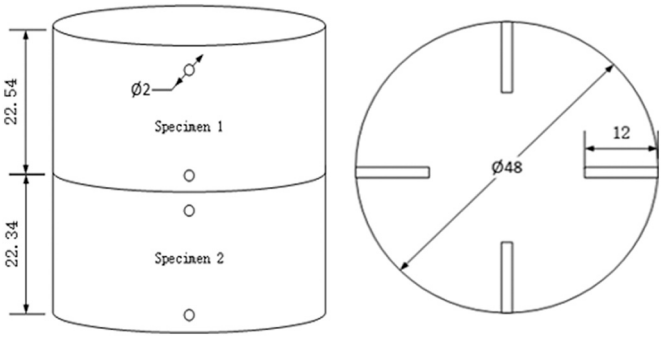

Fig. 7. The specimen schematic.

$$T = Ax + B \tag{4}$$

Where A, B can be obtained by curve fitting the test data. Accordingly, we can calculate the heat flux through the heat flux meter bars and the temperatures of the contact interfaces.

Table 4 shows the heat flux calculated from heat flux meter bars. Since the thermal conductivity of the specimen has been measured, the heat flux can also be approximately obtained from the two measured temperatures of the specimens. It can be seen that all deviations between specimen heat fluxes and meter-bar fluxes are within 13%, which shows the reliability of thermal conductivity measurements in some extent.

(a) The experimental setup for measuring temperature profile

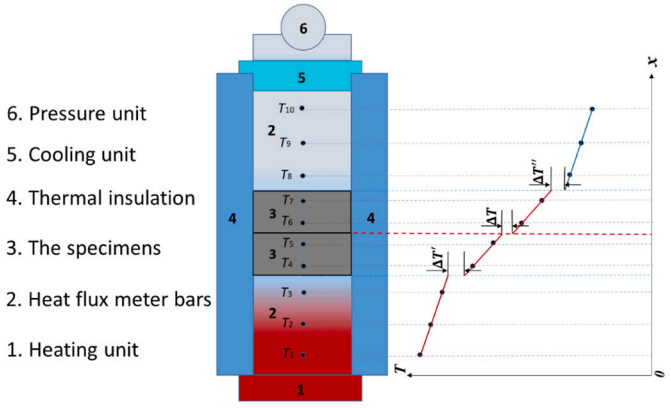

(b) The schematic diagram of the temperature measurement

Fig. 8. The temperature profile measurement.

3.5. Thermal contact resistance

(1) 3DN C/SiC pairs (Contact B in Table 1)

Fig. 14 depicts temperature differences between two composite contact interfaces. An obvious tendency in Fig. 14(a) is that the temperature difference increases with an increase in interface temperature and decreases with an increase in loading pressures. It should be noted that the last temperature case at $p = 3.57$ MPa decreases suddenly. It might be caused by experimental uncertainty of ΔT. To show the actual measurement results, it is kept there as is. Fig. 14 (b) shows thermal contact resistance versus loading pressures and interface average temperatures. It can be seen that the thermal contact resistance decreases with an increase in both interface temperature and loading pressure. Comparing Fig. 14 (a) and (b), we can find that temperature difference increases and thermal contact resistance decreases with an increase in interface average temperature, which is because that thermal contact resistance is determined by temperature difference divided by heat flux, so even when temperature difference increases, thermal contact resistance will decrease when the increment of heat flux is larger than that of the temperature difference (see Fig. 14 (c)). Besides, the effect of temperature on thermal contact resistance gradually decreases with an increasing loading pressure. It is because a larger loading pressure contributes to more actual contact area and enhancing the heat transfer between the contact interfaces. Even though the actual mechanism of contact surface deformation remains a challenging problem, generally

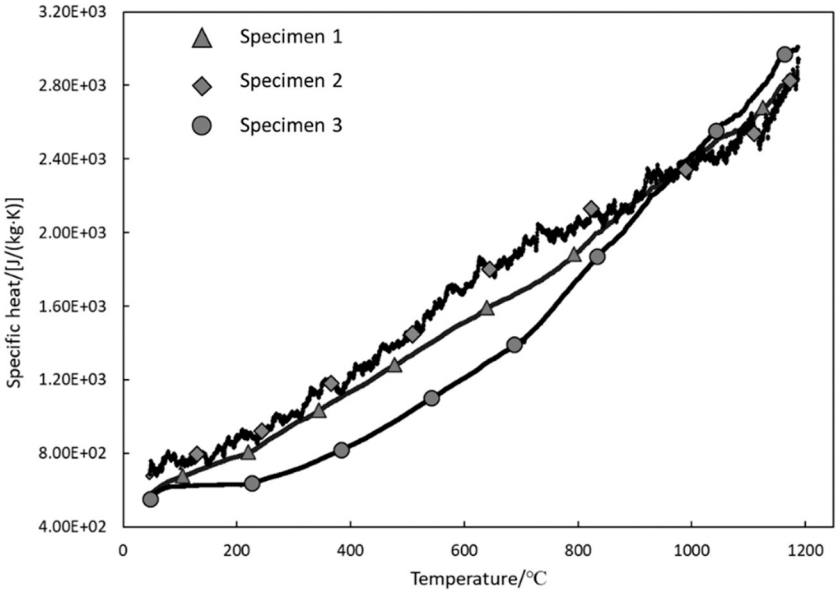

Fig. 9. Specific heat capacity

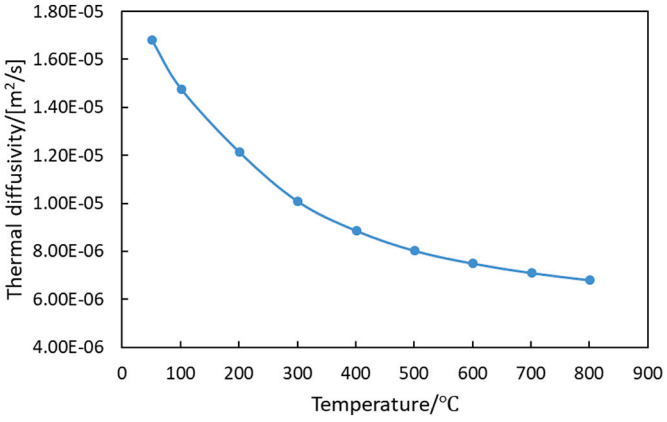

Fig. 10. Thermal diffusivity (through-thickness direction) vs. temperature

speaking, deformation includes three steps: elastic, elastic-plastic and plastic. The elastic deformation must happen firstly, and when pressure increases, elastic-plastic and plastic may happen or not. It can be sure that at a larger pressure the elastic deformation contributes more

Table 2
Three experimental results of the thermal conductivity.

T/°C	λ/[W/(m·K)]				Deviation		
	Laser-flash	ASTM	Hotdisk	Mean value	δ_1	δ_2	δ_3
50.6	24.2	23.5	23.8	23.9	1.5%	−1.3%	−0.1%
101.0	22.5	23.8	24.4	23.6	−4.6%	1.1%	3.5%
200.9	21.8	24.4	25.6	23.9	−8.8%	2.0%	6.9%
300.9	20.5	24.9	26.7	24.0	−14.7%	3.7%	11.0%
400.9	22.1	25.5	27.9	25.1	−12.1%	1.4%	10.7%
501.0	23.3	26.1	29.1	26.1	−10.8%	−0.2%	11.0%
600.9	25.7	26.6	30.2	27.5	−6.5%	−3.2%	9.7%
701.0	27.2	27.2	31.4	28.6	−4.8%	−4.8%	9.6%
801.0	28.5	27.7	32.6	29.6	−3.6%	−6.2%	9.8%

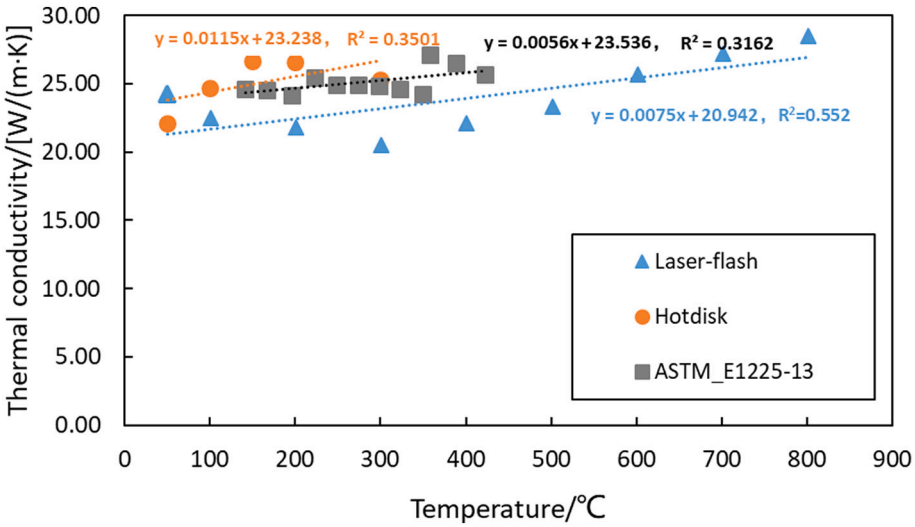

Fig. 11. Thermal conductivity (through-thickness direction) vs. temperature.

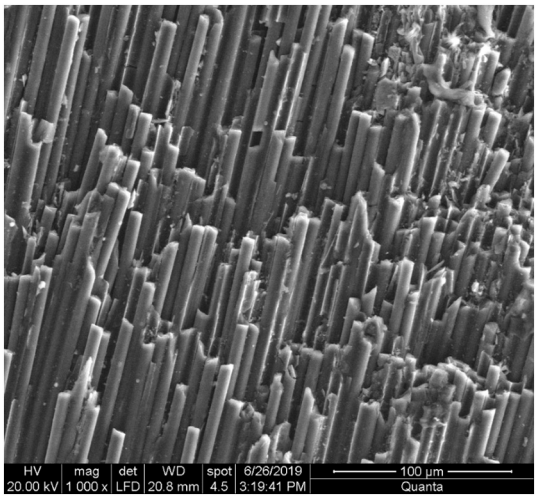

Fig. 12. Internal structure of 3DN C/SiC

Table 3
Experimental conditions.

Heating temperature/°C	400; 450; 500; 550; 600; 650; 700; 800; 900
Loading pressure/MPa	1.48; 1.97; 2.48; 3.57; 4.39
Coolant temperature/°C	15
Criteria for steady state	T changes by <0.3 °C within 0.5 h

contact area.

(2) 3DN C/SiC-TC4 alloy (Contact C in Table 1)

Fig. 15 shows the variation dependency of thermal contact resistance of Contact C on loading pressure and interface average temperature. It can be seen that thermal contact resistance of Contact C decreases with an increase in both interface temperature and loading pressure. Although both Figs. 14 (b) and 15 show thermal contact resistance decreases with an increasing interface temperature, to the authors' knowledge, there isn't a fixed variation tendency on how thermal contact resistance changes with a change in temperature. Because the variation tendency relies on many factors, including materials, roughness, thermal conductivities and experimental conditions, etc. For examples, Joseph et al. [24] showed that thermal contact resistance increased with an increase in temperature at low temperature and steady load, while other studies [2,22] showed that thermal contact resistance decreased with an increase in temperature. Bi et al. [23] even observed that thermal contact resistance of AlN-AlN ceramic initially decreased and then increased with an increase in temperature.

Fig. 16 shows thermal contact resistance dependency of Contact A & C on interface average temperatures under 1.48 MPa. It can be seen that thermal contact resistance of Contact C is larger than that of Contact A. It is because that the sum of the roughness of two contact interfaces in Contact C is higher than that in Contact A. It should be noted that Contacts A and C are both titanium alloy/composite contact pairs, and the only difference is their roughness, however, their TCR values are quite different at the same other test conditions. The results once again show the complexity of thermal contact resistance determination. In addition, there is a large difference between 200 deg. C and 250 deg. C of Contact A. It might be caused by the experimental errors, however, the general trend is decreasing.

4. Uncertainty analysis

4.1. The main sources of the uncertainty

The main uncertainties for determining thermal contact resistance come from temperature difference and heat flux determination according to Eq. (2), and the measurement standard uncertainty calculating for a Type A evaluation can be estimated by Eq. (5) [46],

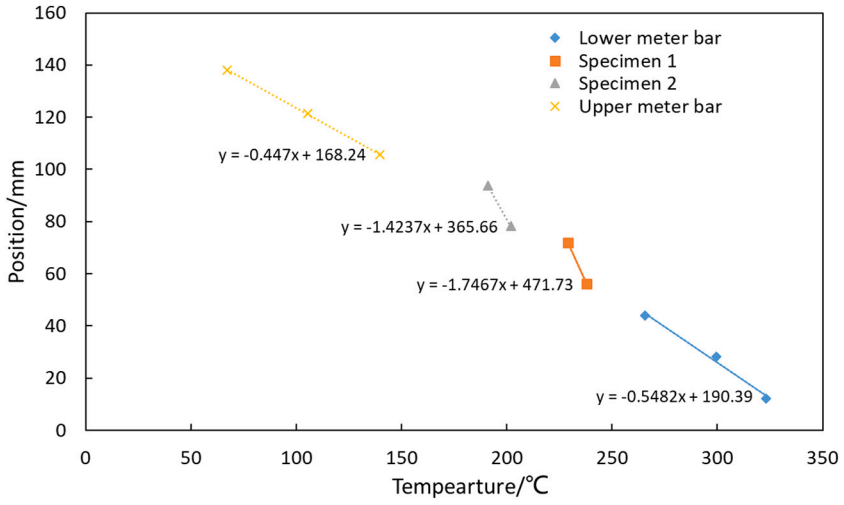

Fig. 13. Temperature profile.

Table 4
Heat flux comparison between heat flux meters and specimens.

Heating temperature/°C	400	450	500	550	600	650	700
q from meter bars/W·m^{-2}	16,940.3	20,912.8	24,007.1	26,838.6	30,062.2	33,277.8	36,653.7
q from specimens /W·m^{-2}	15,430.3	18,554.2	21,743.6	25,315.8	29,230.9	33,186.8	37,797.2
Deviation	9.8%	12.7%	10.4%	6.0%	2.8%	0.3%	−3.0%

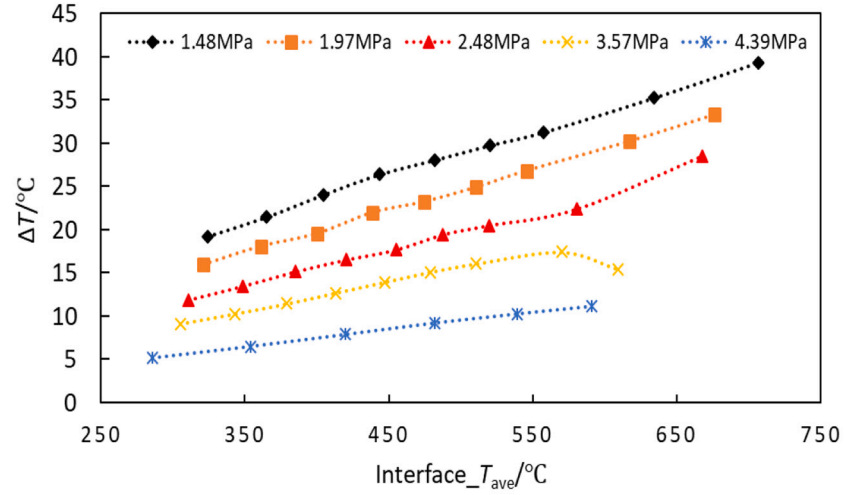

(a) Temperature difference vs. interface temperature

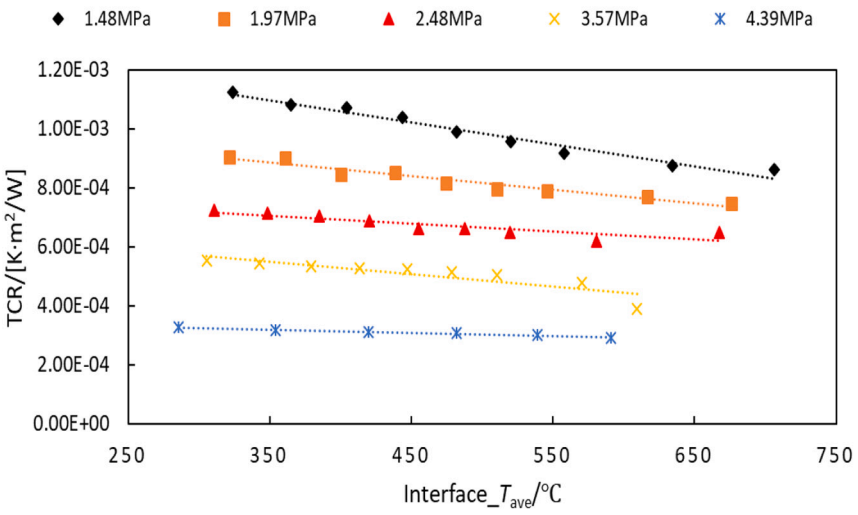

(b) Thermal contact resistance vs. interface temperature

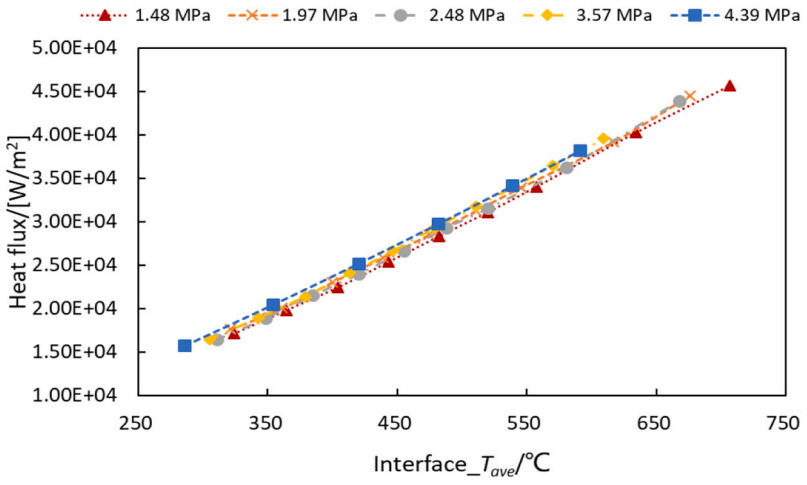

(C) Heat flux

Fig. 14. Temperature difference and thermal contact resistance of Contact B.

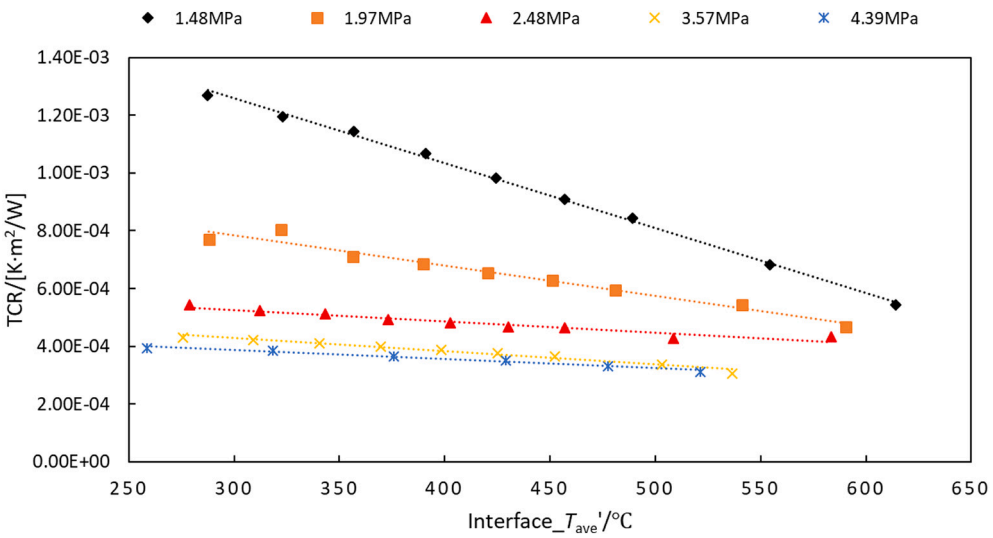

Fig. 15. Thermal contact resistance between 3DN C/SiC and TC4 alloy in Contact C.

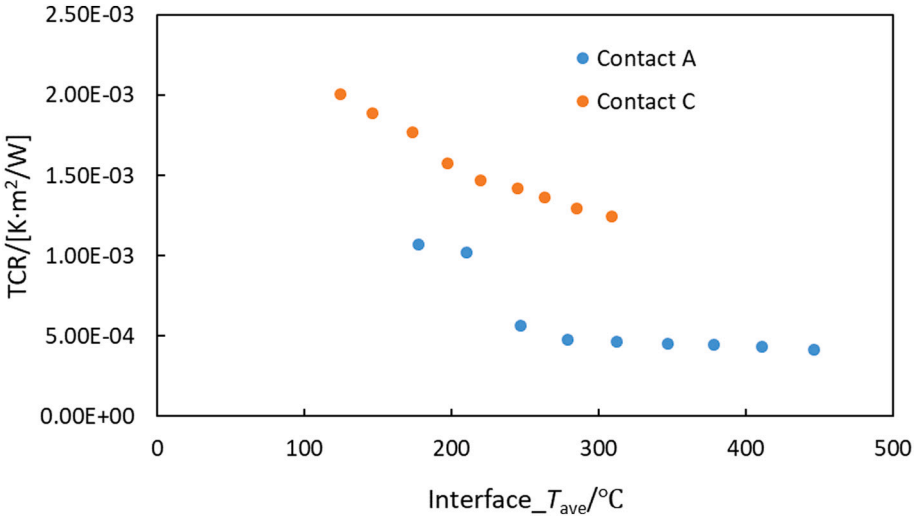

Fig. 16. Thermal contact resistance between 3DN C/SiC and TC4 alloy under 1.48 MPa

$$u(R) = \sqrt{\frac{1}{q^2}u(\Delta T)^2 + \frac{(\Delta T)^2}{q^4}u(q)^2} \tag{5}$$

where $u(R)$ denotes the standard uncertainty of R; $u(\Delta T)$ and $u(q)$ denote the standard uncertainties of ΔT and q, respectively. The detailed process for calculating $u(\Delta T)$ and $u(q)$ can be illustrated as follows,

(1) $\Delta T = T$ - $T^+$is the temperature difference between two contact interfaces, so $u(\Delta T)$ can be written as Eq. (7),

$$u(\Delta T) = \sqrt{u(T^-)^2 + u(T^+)^2} \tag{7}$$

where, $T^+$and $T^-$are the temperatures of top contact interface and bottom contact interface respectively. For temperature measurement under steady state, the experimental temperature uncertainty can be evaluated by Eq. (8),

$$u(T) = \sqrt{\frac{\sum_{i=1}^{n}\left(T_i - \overline{T}\right)^2}{n(n-1)}} \tag{8}$$

where, T_i is the temperature of single measurement, and $\overline{T}$ is the average value of n single measurements. During our test run 10 single measurement values under steady state within 30 min were recorded, hence n takes a value of ten. It should be mentioned that here the thermal contact resistances between thermocouples and specimens are neglected. Besides, $T^+$and $T^-$are obtained by linear fitting method, so Eq. (9) can be used,

$$u(T) = u(T^-) = u(T^+) \tag{9}$$

(2) q is the heat flux calculated by the measured temperatures and known thermal conductivity of heat flux meter bars according to the Fourier's law of heat conduction,

$$q = -\lambda\frac{T_{x_2} - T_{x_1}}{\Delta x} \tag{10}$$

where, Δx is the distance between two measurement spots (x_1 and x_2) and can be regarded as a constant; $T_{x1}$and $T_{x2}$are temperatures at x_1 and x_2 spots of heat flux meter bar respectively. Then we have,

Table 5
Uncertainties.

T	P								
	1.48 MPa			2.48 MPa			4.39 MPa		
	$R/10^{-5}$ $K{\cdot}m^2{\cdot}W^{-1}$	$u(R)/10^{-5}$ $K{\cdot}m^2{\cdot}W^{-1}$	$U(R)$	$R/10^{-5}$ $K{\cdot}m^2{\cdot}W^{-1}$	$u(R)/10^{-5}$ $K{\cdot}m^2{\cdot}W^{-1}$	$U(R)$	$R/10^{-5}$ $K{\cdot}m^2{\cdot}W^{-1}$	$u(R)/10^{-5}$ $K{\cdot}m^2{\cdot}W^{-1}$	$U(R)$
400	112.4	6.4	5.7%	72.3	6.4	8.9%	32.7	6.2	18.9%
500	107.0	6.3	5.9%	70.3	6.2	8.9%	31.7	6.0	19.1%
600	99.0	5.8	5.9%	66.3	5.8	8.8%	31.2	5.7	18.2%
700	91.8	5.6	6.1%	65.0	5.6	8.6%	30.8	5.5	17.9%
800	87.5	5.4	6.2%	61.8	5.5	8.9%	30.0	5.4	18.0%
900	86.1	5.3	6.2%	64.9	5.2	8.0%	29.2	5.3	18.1%

$$u(q) = \sqrt{\left(\frac{\lambda_m}{\Delta x}\right)^2 \left[u(T_{x_2})^2 + u(T_{x_1})^2\right]} \tag{11}$$

where λ_m is the average thermal conductivity of heat flux meter bar, and $u(T_{x1})$ and $u(T_{x2})$ can be calculated by Eq. (8).

4.2. Uncertainty calculation

The cases of 400, 500, 600, 700, 800 and 900 °C under 1.48, 2.48 and 4.39 MPa are selected to calculate experimental uncertainties, and the results are listed in Table 5. The results show that the standard uncertainty u(R) at pressure of 1.48 MPa and 2.48 MPa are within 10%, and still keeps below 20% when pressure loading increases 4.39 MPa. It is because that thermal contact resistance R decreases with an increasing loading pressure.

5. Conclusions

This paper conducts experimental study for thermal contact resistance of three pairs (A,B,and C) of carbon fiber reinforced silicon carbide composites with 3D needled preform (3DN C/SiC). For determining thermal conductivity, thermal diffusivity and specific heat capacity of the composite are experimentally measured. The two surfaces of Contact B are both needled composite, while Contacts A and C are composed by Titanium alloy and needled composite. The surface roughnesses of the three contacts are 0.95/16.91 μm, 9.54/9.73 μm, and 11.53/6.85 μm, respectively. The measured results can be summarized as follows:

1. The TCR ranges of Contacts A, B, and C are 4.13×10^{-4}-1.08×10^{-3} $K{\cdot}m^2{\cdot}W^{-1}$, 2.92×10^{-4}-1.27×10^{-3} $K{\cdot}m^2{\cdot}W^{-1}$, and 3.1×10^{-4}-1.3×10^{-3} $K{\cdot}m^2{\cdot}W^{-1}$, respectively. The corresponding test ranges of Contact A, B and C are (450–720) K/1.48 MPa, (560–980) K/(1.48–4.39) MPa, and (530–885) K/(1.48–4.39) MPa, respectively.
2. The measured TCRs of the three contacts decreases with the increase in loading pressure and interface temperature.
3. For Contact C when loading pressure increases to 3.6 MPa, the decreasing trend of the thermal contact resistance with increasing loading pressure becomes mild. For both Contacts B and C, the effect of temperature on thermal contact resistance also decreases when loading pressure increases.

Credit author statement

Xing-Jie Ren: Conceptualization, Investigation, Methodology, Writing - Original Draft, Writing - Review & Editing. **Hao Ding**: Investigation. **Yan-Jun Dai**: Funding acquisition. **Jian-Yong Tu**: Resources. **Xu Chen**: Resources. **Jiang-Yi He**: Resources. **Wen-Quan Tao**: Funding acquisition, Supervision.

Declaration of Competing Interest

None.

Acknowledgement

This study is supported by the National Natural Science Foundation of China (51806167), The fund of Xi'an Science & Technology Bureau (2019218714SYS002CG024) and 111 Project (B16038).

References

[1] M.M. Yovanovich, Four decades of research on thermal contact, gap, and joint resistance in microelectronics, Ieee Trans. Comp. Pack. Tech. 28 (2) (2005) 182–206.
[2] Y.J. Dai, J.J. Gou, X.J. Ren, et al., A test-validated prediction model of thermal contact resistance for Ti-6Al-4V alloy, Appl. Energy 228 (2018) 1601–1617.
[3] T. Barratt, The magnitude of the thermal resistance introduced at the slightly conical junction of two solids, and its variation with the nature of the surfaces in contact, Proc. Phys. Soc. Lond. 28 (1916) 0014–0020.
[4] J.A. Greenwood, J.B.P. Williamson, Contact of nominally flat surfaces, Proc. Royal Soc. A: Math. Phys. Eng. Sci. 295 (1442) (1966) 300–319.
[5] L.S. Fletcher, P.A. Smuda, D.A. Gyorog, Thermal contact resistance of selected low-conductance interstitial materials, AIAA J. 7 (7) (1969), pp. 1302-&.
[6] B.B. Mikic, Thermal contact conductance - theoretical considerations, Int. J. Heat Mass Transf. 17 (2) (1974) 205–214.
[7] A. Bush, R. Gibson, T. Thomas, The elastic contact of a rough surface, Wear 35 (1) (1975) 87–111.
[8] J.I. McCool, Comparison of models for the contact of rough surfaces, Wear 107 (1) (1986) 37–60.
[9] B.N.J. Persson, Elastoplastic contact between randomly rough surfaces, Phys. Rev. Lett. 87 (11) (2001).
[10] S.M.S. Wahid, C.V. Madhusudana, Thermal contact conductance: effect of overloading and load cycling, Int. J. Heat Mass Transf. 46 (21) (2003) 4139–4143.
[11] J. Greenwood, A simplified elliptic model of rough surface contact, Wear 261 (2) (2006) 191–200.
[12] G. Carbone, F. Bottiglione, Asperity contact theories: do they predict linearity between contact area and load? J. Mech. Phys. Solids 56 (8) (2008) 2555–2572.
[13] B. Salti, N. Laraqi, 3-D numerical modeling of heat transfer between two sliding bodies: temperature and thermal contact resistance, Int. J. Heat Mass Transf. 42 (13) (1999) 2363–2374.
[14] A.S. Marchand, N. Raynaud, Numerical determination of thermal contact resistance for nonisothermal forging processes, J. Heat Transf. Trans. Asme 122 (4) (2000) 776–784.
[15] X. Zhang, P.Z. Cong, S. Fujiwara, et al., A new method for numerical simulation of thermal contact resistance in cylindrical coordinates, Int. J. Heat Mass Transf. 47 (5) (2004) 1091–1098.
[16] F.B. Hsiao, D.B. Wang, C.P. Jen, Numerical investigation of thermal contact resistance between the mold and substrate on laser-assisted imprinting fabrication, Num. Heat Trans. Part A-Appl. 49 (7) (2006) 669–682.
[17] J.-J. Gou, X.-J. Ren, Y.-J. Dai, et al., Study of thermal contact resistance of rough surfaces based on the practical topography, Comput. Fluids 164 (2018) 2–11.
[18] X.-J. Ren, Y.-J. Dai, J.-J. Gou, et al., Numerical prediction of thermal contact resistance of 3D C/C-SiC needled composites based on measured practical topography, Int. J. Heat Mass Transf. 131 (2019) 176–188.
[19] G. Karimi, X. Li, P. Teertstra, Measurement of through-plane effective thermal conductivity and contact resistance in PEM fuel cell diffusion media, Electrochim. Acta 55 (5) (2010) 1619–1625.
[20] V. Gopal, M.J. Whiting, J.W. Chew, et al., Thermal contact conductance and its dependence on load cycling, Int. J. Heat Mass Transf. 66 (2013) 444–450.
[21] P. Zhang, Y. Xuan, Q. Li, A high-precision instrumentation of measuring thermal contact resistance using reversible heat flux, Exp. Thermal Fluid Sci. 54 (2014) 204–211.
[22] R.F. Dou, T.R. Ge, X.L. Liu, et al., Effects of contact pressure, interface temperature, and surface roughness on thermal contact conductance between stainless steel surfaces under atmosphere condition, Int. J. Heat Mass Transf. 94 (2016) 156–163.
[23] B. Dongmei, C. Huanxin, L. Shanjian, et al., Measurement of thermal diffusivity/thermal contact resistance using laser photothermal method at cryogenic temperatures, Appl. Therm. Eng. 111 (2017) 768–775.

[24] R. Joseph, J. Peter, S.S. Kumar, et al., Effect of thermal and load cycle on thermal contact conductance across dissimilar joints at cryogenic temperature, Appl. Therm. Eng. 111 (2017) 1622–1628.
[25] P. Zhang, T. Cui, Q. Li, Effect of surface roughness on thermal contact resistance of aluminium alloy, Appl. Therm. Eng. 121 (2017) 992–998.
[26] J.E. Cousineau, K. Bennion, D. DeVoto, et al., Experimental characterization and modeling of thermal resistance of electric machine lamination stacks, Int. J. Heat Mass Transf. 129 (2019) 152–159.
[27] V.T. Le, N.S. Goo, J.Y. Kim, Experimental investigation on thermal contact resistance of alumina fibrous insulation material with Ti-6Al-4V alloy at high temperature and its effective thermal conductivity, Heat Mass Transf. 55 (6) (2019) 1705–1721.
[28] Q.-Y. Li, K. Katakami, T. Ikuta, et al., Measurement of thermal contact resistance between individual carbon fibers using a laser-flash Raman mapping method, Carbon 141 (2019) 92–98.
[29] A.T. Vu, T. Helmig, A.N. Vu, et al., Numerical and experimental determinations of contact heat transfer coefficients in nonisothermal glass molding, J. Am. Ceram. Soc. 103 (2) (2019) 1258–1269.
[30] E.M. Burghold, Y. Frekers, R. Kneer, Determination of time-dependent thermal contact conductance through IR-thermography, Int. J. Therm. Sci. 98 (2015) 148–155.
[31] E.M. Burghold, Y. Frekers, R. Kneer, Transient contact heat transfer measurements based on high-speed IR-thermography, Int. J. Therm. Sci. 115 (2017) 169–175.
[32] Z. Zhu, L. Zhang, C. Zhang, et al., Experimental investigation of transient contact heat transfer between 300M and 5CrNiMo, Int. J. Heat Mass Transf. 96 (2016) 451–457.
[33] ASTM, Standard Test Method for Thermal Transmission Properties of Thermally Conductive Electrical Insulation Materials, 2012.
[34] D. Toebben, H. Schulte, P. Luczynski, et al., Experimental investigation of the oxidation influence on the thermal contact resistance at the blade-rotor-connection in a steam turbine, in: International Heat Transfer Conference Digital Library, Begel House Inc, 2018.
[35] A. Tariq, M. Asif, Experimental investigation of thermal contact conductance for nominally flat metallic contact, Heat Mass Transf. 52 (2) (2016) 291–307.
[36] Y. Benveniste, Effective thermal conductivity of composites with a thermal contact resistance between the constituents: nondilute case, J. Appl. Phys. 61 (8) (1987) 2840–2843.
[37] V.V. Rao, M.V.K. Murthy, J. Nagaraju, Thermal conductivity and thermal contact conductance studies on Al2O3/Al-AlN metal matrix composite, Compos. Sci. Technol. 64 (16) (2004) 2459–2462.
[38] P. Zhang, Q. Li, Y.M. Xuan, Thermal contact resistance of epoxy composites incorporated with nano-copper particles and the multi-walled carbon nanotubes, Comp. Part a-Appl. Sci. Manufact. 57 (2014) 1–7.
[39] ASTM, Standard Test Method for Thermal Conductivity of Solids Using the Guarded-Comparative-Longitudinal Heat Flow Technique, ASTM International, West Conshohocken, PA, 2013.
[40] J.-J. Gou, H. Zhang, Y.-J. Dai, et al., Numerical prediction of effective thermal conductivities of 3D four-directional braided composites, Compos. Struct. 125 (2015) 499–508.
[41] N.P. Bansal, Handbook of Ceramic Composites Vol. 200, Springer Science & Business Media, 2006.
[42] S. Kumar, A. Kumar, A. Shukla, et al., Thermal-diffusivity measurement of 3D-stitched C–SiC composites, J. Eur. Ceram. Soc. 29 (3) (2009) 489–495.
[43] J.-J. Gou, Y.-J. Dai, S. Li, et al., Numerical study of effective thermal conductivities of plain woven composites by unit cells of different sizes, Int. J. Heat Mass Transf. 91 (2015) 829–840.
[44] J.J. Gou, X.J. Ren, W.Z. Fang, et al., Two small unit cell models for prediction of thermal properties of 8-harness satin woven pierced composites, Comp. Part B-Eng. 135 (2018) 218–231.
[45] S. Yeo, R. Baney, G. Subhash, et al., The influence of SiC particle size and volume fraction on the thermal conductivity of spark plasma sintered UO2–SiC composites, J. Nucl. Mater. 442 (1–3) (2013) 245–252.
[46] R. Kempers, P. Kolodner, A. Lyons, et al., A high-precision apparatus for the characterization of thermal interface materials, Rev. Sci. Instrum. 80 (9) (2009), 095111.